Proceedings of ASME Turbo Expo 2015: Turbine Technical Conference and Exposition
GT2015
June 15-19, 2015, Montreal, Canada

DRAFT

GT2015-42773

DNS OF FLOW IN A LOW-PRESSURE TURBINE CASCADE USING A DISCONTINUOUS-GALERKIN SPECTRAL-ELEMENT METHOD

Anirban Garai
Oak Ridge Associated Universities
NASA Ames Research Center
Moffett Field, CA, USA

Laslo Diosady
Science and Technology Corporation
NASA Ames Research Center
Moffett Field, CA, USA

Scott Murman
NASA Ames Research Center
Moffett Field, CA, USA

Nateri Madavan
NASA Ames Research Center
Moffett Field, CA, USA

ABSTRACT

A new computational capability under development for accurate and efficient high-fidelity direct numerical simulation (DNS) and large eddy simulation (LES) of turbomachinery is described. This capability is based on an entropy-stable Discontinuous-Galerkin spectral-element approach that extends to arbitrarily high orders of spatial and temporal accuracy and is implemented in a computationally efficient manner on a modern high performance computer architecture. A validation study using this method to perform DNS of flow in a low-pressure turbine airfoil cascade are presented. Preliminary results indicate that the method captures the main features of the flow. Discrepancies between the predicted results and the experiments are likely due to the effects of freestream turbulence not being included in the simulation and will be addressed in the final paper.

NOMENCLATURE

C	Axial chord length
E	Total energy
$\boldsymbol{F}$	Flux vector
H	Enthalpy
$\boldsymbol{L}$	Left Eigenvector of the flux Jacobian
Ma	Mach number
$\boldsymbol{Q}$	Entropy variable
$\boldsymbol{R}$	Right Eigenvector of the flux Jacobian
Re	Reynolds number
T	Temperature
U	Speed
a	Speed of sound
$\boldsymbol{n}$	Normal direction
p	Pressure
$\boldsymbol{q}$	Conservative variable
s	Entropy
t	Time
$\boldsymbol{v}$	Velocity vector
w	Basis function
x	Coordinate direction
y	Coordinate direction
z	Coordinate direction
$\boldsymbol{\Lambda}$	Eigenvalues of the flux Jacobian
β	Flow angle
γ	Specific gas constant
δ	Boundary-layer thickness
η	Wall-normal direction
κ	Thermal conductivity
λ	Bulk viscosity
μ	Viscosity
ξ	Tangential direction
ρ	Density

τ	Viscous stress
Superscripts	
I	Inviscid
V	Viscous
Subscripts	
1	Inlet
2	Exit
is	Isentropic
n	Surface normal
t	Total properties

INTRODUCTION

The numerical simulation of turbomachinery flows is a challenging problem for Computational Fluid Dynamics. These flows involve both complex physics, such as wake impingement upon blades, and acoustics, along with complex moving geometries to resolve the tight clearances between components, especially near the tip region.

Over the past several decades, turbomachinery flow simulation capability has advanced from the early one-dimensional, steady, inviscid and viscous approximations to steady and unsteady two- and three-dimensional approaches capable of solving the Reynolds-Averaged Navier-Stokes equation (RANS) in multistage settings. The current RANS-based methods have proven extremely useful, although their inherent limitations in modeling transitional and turbulent flows in complex configurations are well recognized. In recent years, the rapid expansion of high performance computing capability has led to attention being focused on high fidelity simulation techniques, such as DNS and LES. These techniques offer the promise of more accurate and better resolved simulations that can shed more light on the complicated flow phenomena and lead to improved turbomachinery designs.

There are several studies reported in the recent literature on applying DNS and LES techniques to turbomachinery applications. Using incompressible DNS methods, Wu and Durbin [1], Wissink and coworkers (see, for example, [2], [3]) studied flow transition in turbine cascades due to freestream turbulence and incoming wakes, and Zaki et al. [5] studied the effect of freestream turbulence in a compressor cascade. Rai applied compressible DNS techniques in conjunction with overset-grid techniques to simulate transitional flow in a turbine stator passage [6]; these techniques were later extended to turbine and compressor stage configurations [7-9] where the effects of rotor-stator interaction were studied. More recently, Sandberg et al. [10] and Michelassi et al. [11] have reported efficient DNS simulations of a low-pressure turbine cascade. All these simulations were performed on idealized mid-span configurations and at low Reynolds number in order to keep computational resources reasonable. Note that these references are representative but by no means represent the entire body of prior work that has been reported in this area. In addition to DNS studies, several researchers have focused on the application of LES methods. Michelassi et al. [12] performed LES of turbine cascades at conditions that match reference DNS data. The influence of freestream turbulence on transition in turbine and compressor blading has been investigated using LES by Raverdy et al. [13], Matsuura and Kato [14], Sarkar and Voke [15], Medic and Sharma [16], and others. In addition to these efforts, DNS and LES techniques have also been successfully used to study other turbomachinery flow features, such as tip clearance flows [17], noise generation due to entropy waves [18], and blade cooling effects.

Many of the studies in the literature have made use of high-order spatial finite-difference and finite-volume techniques because of their superiority in resolving a wide range of spatial and temporal scales using coarser meshes compared to traditional second-order methods. For example, Sandberg et al. [10] and Michelassi et al. [11] used fourth-order compact finite difference schemes to study the effect of freestream turbulence on the transitional flow in a turbine cascade, while Rai [6-9] made use of high-order upwind-biased schemes.

There is growing interest in the development and use of Discontinuous-Galerkin (DG) methods due to their attractive features for high-accuracy numerical simulations of a variety of fluid flow configurations. In addition to the ability to formulate arbitrarily high-order schemes while maintaining a compact numerical stencil, DG methods are extremely flexible and can handle a variety of element types and mesh topologies. They are thus computationally efficient, and also allow a number of adaptation techniques and solver acceleration strategies to be implemented in a straightforward manner. For these reasons, these methods have become the focus of recent research. In the past few years, these methods are being evaluated for turbomachinery applications. Work on RANS-based turbomachinery simulations using DG methods was first reported by Bassi et al. [19] and, more recently, in Refs. [20-22]. DNS simulations of turbomachinery configurations using these methods have recently been reported by de Wiart et al. [23] and Hillewaert et al. [24]. The results presented in this paper represent research work in this direction.

This paper describes a new computational capability for accurate and efficient high-fidelity direct numerical simulations (DNS) and large eddy simulations (LES) for turbomachinery applications. This capability is based on an entropy-stable Discontinuous Galerkin spectral-element approach for compressible flows that extends to arbitrarily high orders of spatial and temporal accuracy and is implemented in a computationally efficient manner on a modern high performance computer architecture. This capability will advance turbomachinery flow simulation beyond the current reliance on steady and unsteady RANS methods with their inherent limitations. It will serve as a valuable analysis tool to understand complicated flow phenomena, such as rotor-stator interaction and tip clearance effects, and will ultimately help lead to improved turbomachinery designs where their detrimental effects on performance and operability are mitigated.

As a first step towards a general capability, the DNS of transitional and turbulent flow in a turbine stator cascade using an entropy-stable DG spectral-element method are presented in

this paper. The method has previously been validated using simulations of Taylor-Green vortex evolution, compressible channel flow, and the flow over periodic hills [25, 26]. A variational multiscale method (a reformulation of the classical LES formulation) is implemented [27] that also allows the simulation of high-Reynolds number compressible flows where DNS is impractical and RANS-based approaches are inadequate. Here, the method is extended for turbomachinery applications, and validation results are presented for flow in a turbine-stator passage. The flow configuration is the T106D-EIZ low-pressure turbine (LPT) cascade that has been the subject of many experimental and numerical simulation studies [28]. The main objective of this paper is to provide a preliminary validation of the present methodology and demonstrate its future potential in predicting challenging turbomachinery flow phenomena and addressing the needs of the turbulence modeling community in their efforts to improve RANS-based capabilities. The final paper will include additional numerical results, including grid resolution and freestream turbulence effects, and additional details regarding the transient behavior of the transitional flow.

NUMERICAL METHOD

The compressible Navier-Stokes equations are solved for an ideal gas with constant specific heat coefficients in an entropy stable formulation. The Navier-Stokes equations in conservative form can be written as:

$$\boldsymbol{q}_{,t} + (\boldsymbol{F}_i^I + \boldsymbol{F}_i^V)_i = 0, \qquad (1)$$

where, $\boldsymbol{q} = [\rho,\ \rho\boldsymbol{v}, \rho E]$ is the conservative state vector, $\boldsymbol{F}^I = [\rho\boldsymbol{v},\ \rho\boldsymbol{v}\boldsymbol{v} + p\boldsymbol{I},\ \rho\boldsymbol{v}H]$ is the inviscid flux vector and $\boldsymbol{F}^V = [0,\ \boldsymbol{\tau},\ \boldsymbol{v}\cdot\boldsymbol{\tau} + \kappa_T\nabla T]$ is the viscous flux, with $\boldsymbol{\tau} = \mu(\nabla\boldsymbol{v} + \nabla\boldsymbol{v}^T) - \mu\lambda(\nabla\cdot\boldsymbol{v})I$.

Transforming from conservative to entropy variables, $\boldsymbol{q} = \boldsymbol{q}(\boldsymbol{Q})$, Eqn. (1) takes the form:

$$A_0\boldsymbol{Q}_{,t} + A_i\boldsymbol{Q}_{,i} - \left(K_{ij}\boldsymbol{Q}_{,x_j}\right)_{,i} = 0, \qquad (2)$$

with symmetric $A_0 = \boldsymbol{q}_{\boldsymbol{Q}}$, $A_i = \boldsymbol{F}^I_{i,\boldsymbol{q}}A_0$, and $K_{ij} = \boldsymbol{F}^V_{i,\boldsymbol{q}_{,x_j}}A_0$; Here, the entropy variables are given as:

$$\boldsymbol{Q} = \left[-\frac{s}{\gamma-1} + \frac{\gamma+1}{\gamma-1} - \frac{\rho E}{p}, \frac{\rho v}{p}, -\frac{\rho}{p}\right],$$

where entropy is $s = \log\left(\frac{p}{\rho^\gamma}\right)$ (see [29] for more details).

The Navier-Stokes equations in entropy form, as represented by Eqn. (2), are then discretized using a space-time discontinuous Galerkin (DG) finite-element formulation. The spatial domain is partitioned using non-overlapping hexahedral elements (κ), and the time domain is partitioned into time intervals ($I^n = [t^n, t^{n+1}]$). Assuming piecewise polynomial functions in both space and time, Eqn. (2) can be written in weak form as:

$$\sum_\kappa \left\{ \int_I \int_\kappa -\left(\boldsymbol{w}_{,t}\boldsymbol{q} + \boldsymbol{w}_{,i}(\boldsymbol{F}_i^I + \boldsymbol{F}_i^V)\right) + \int_I \int_{\partial\kappa} \boldsymbol{w}\left(\widehat{\boldsymbol{F}_i^I n_i} + \widehat{\boldsymbol{F}_i^V n_i}\right) + \int_\kappa \left(\boldsymbol{w}(t_-^{n+1})\boldsymbol{q}(t_-^{n+1}) - \boldsymbol{w}(t_+^n)\boldsymbol{q}(t_+^n)\right)\right\} = 0 \qquad (3)$$

where, $\boldsymbol{w}$ is the Lagrange basis function defined at Gauss-Legendre points. The inviscid numerical fluxes, $\widehat{\boldsymbol{F}_i^I n_i}$, and viscous numerical fluxes, $\widehat{\boldsymbol{F}_i^V n_i}$, across the jump are calculated using Ismail and Roe's flux [30] and the Bassi and Rebay diffusion operator [31], respectively. Integrals in Eqn. (3) are approximated with a quadrature rule using twice the number of quadrature points as solution points in each coordinate direction in order to minimize quadrature errors. The resulting nonlinear system of equations is then solved using a preconditioned Jacobian-free Newton-Krylov solver. Further details regarding the numerical method can be found in Refs. [25] and [26].

The improved efficiency of the high-order scheme for turbulent flows was demonstrated in [26]. Figure 1, reproduced from [26], shows the error in the kinetic energy balance for the Taylor-Green vortex evolution. The 8th-order scheme provides order-of-magnitude reductions in computational cost to achieve the same error tolerance over the lower-order schemes. The goal of the present effort is to bring these efficiencies to turbomachinery simulations.

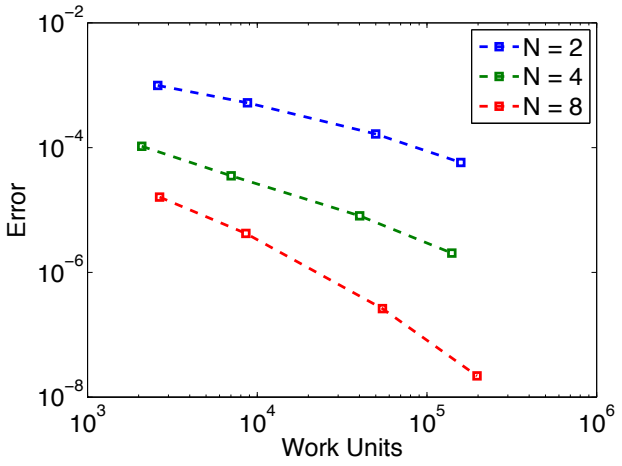

Figure 1. Error in kinetic energy balance as a function of normalized CPU time for Taylor-Green vortex simulation using the present method [26].

EXPERIMENTAL SETUP AND FLOW CONDITIONS

The T106D-EIZ low-pressure turbine cascade configuration experimentally studied by Stadtmuller and Fottner [27] is considered in the present study. The airfoil profile represents the mid-span section of PW2037 rotor blade. In the experimental studies, the blade pitch to chord (the blade chord length is 100 mm) ratio was increased to 1.05 from 0.799

of the original T106A airfoil cascade, in order to achieve a higher blade loading. The experiments were performed both with and without upstream moving cylindrical bars (to simulate the wakes generated from an upstream airfoil row), and for exit Reynolds numbers ranging from 60,000 to 200,000. In the present study, the case without the upstream moving bars with an exit Reynolds number of 200,000 is chosen to validate the numerical methodology, due to the availability of better quality experimental data. The operating conditions for the selected test case are shown in Table 1, and geometrical details of the experimental configuration are shown in Fig. 2. The inflow angle, β_1, in the experiment differed from the geometric flow angle, and we have used β_1=131.6° to be consistent with the previously reported RANS simulations [32] for the same test case. We note also that we have chosen this configuration of the T106 geometry instead of the lightly loaded T106A geometry that has been widely studied in the past because it represents a much more difficult and challenging testcase.

Exit Reynolds number, Re_2	200,000
Exit Mach number, Ma_2	0.4
Total pressure, p_t	259.6 hPa
Static pressure at inlet, p_1	242.5 hPa
Static pressure at exit, p_2	232.6 hPa
Total temperature, T_t	40 °C
Inflow turbulence level	≈ 2.5%

Table 1. Operating conditions for the selected test case.

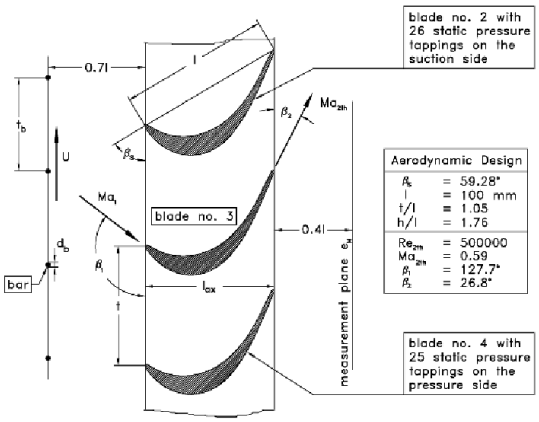

Figure 2. Geometrical details of the T106D-EIZ cascade [28].

COMPUTATIONAL DETAILS

In order to handle the complex geometry of turbomachinery configurations at arbitrarily high order accuracy, the spectral isoparametric mapping demonstrated in [26] is extended to multiblock configurations. The 2D representation of the cascade passage discretized using a multiblock approach is illustrated in Fig. 3. Each individual block uses a separate isoparametric mapping, with the faces between each block handled as DG element interfaces. In this manner, any combination of number of elements and element order can be used within each grid block.

In the region adjacent to the blade, an O-grid topology is used up to twice the boundary-layer thickness (at the 0.9930*C* location, where *C* is the axial chord length) in the wall-normal direction, and an H-grid topology is used on the rest of the blade passage. The airfoil O-grid is then partitioned into 6 different blocks to match the neighboring H-blocks. The 2D grid is extruded in the spanwise direction to generate the 3D grid. The spanwise extent of the computational domain is chosen as 20% of the chord length. This spanwise extent was deemed to be sufficient for capturing the largest turbulent scales based on other DNS simulations of LPT cascades with similar geometries but different airfoil pitch reported in the literature [1, 5].

Spectral elements are generated for each grid from this multiblock grid. For the blocks adjacent to the airfoil, eight elements are used in the wall-normal direction; the height of the first element near the wall is 0.002*C* and the elements are uniformly stretched in the wall-normal direction. This results in the wall-normal extent of the first element near the wall being roughly 10-20 wall units on the suction side of the airfoil. Along the blade surface (tangential direction), the element size is varied from 0.0066*C* to 0.049*C* on the suction side, and from 0.01*C* to 0.23*C* on the pressure side with clustering used in the leading and trailing edge regions. Coarser elements are used on the pressure side compared to the suction side, since for the test case considered the flow is laminar on the pressure side. To resolve the trailing edge wake, elements of size about 0.058*C* in the flow direction and 0.07*C* in the flow normal direction are used and extending downstream up to about two chord lengths from the trailing edge. The inflow and outflow boundaries are located about 2.9*C* and 4*C* from the leading and trailing edge, respectively. Eight elements are used in the spanwise direction, resulting in the spanwise extent of a single element being 0.029*C*. This results in a total of 8528 elements in the airfoil passage.

Figure 4 shows the nodal locations for 2nd, 4th and 8th-order elements with 0.068M, 0.55M, and 4.3M degrees of freedom, respectively, for a single blade passage.

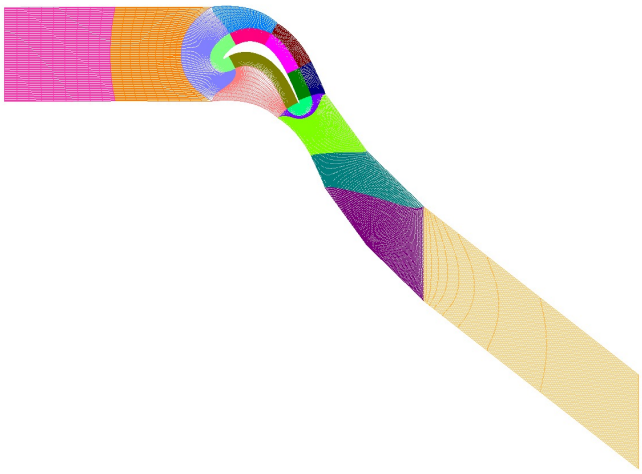

Figure 3. Discretized blade passage using multiblock approach. Different colors in the figure represent different blocks.

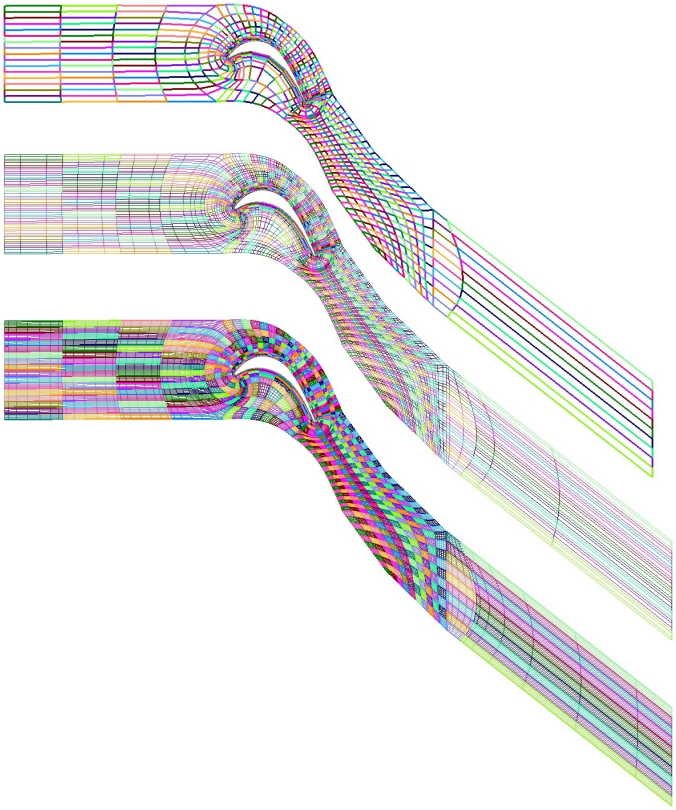

Figure 4. Computational mesh used to represent the airfoil passage. The top, middle, and bottom figures denote 2nd, 4th and 8th order elements, and different colors are used to represent individual elements.

RESULTS

In the current simulations, elements that are 2nd, 4th and 8th-order in space and 4th-order in time are used with a convective CFL number of 5. The simulations are carried out for a total of 14 flow-through times, where the flow-through time is defined by $C/Ma_1 a_1$. Flow statistics are then calculated by averaging over the last four flow-through times.

Periodic boundary conditions are used in the pitchwise and spanwise direction. On the airfoil surface, a no-slip adiabatic wall boundary condition is used. At the inflow and outflow boundaries, boundary normal velocity, pressure and density are evaluated by solving a 1D Riemann problem between the reservoir and local conditions at the boundary. The velocity vector at the inflow is specified from the experimental flow angle. The experimental inflow and outflow conditions (see Table 1) are used to represent the reservoir conditions. Although the freestream turbulence level in the experiment is 2.5%, we have simulated the experimental cascade with zero inflow turbulence as an initial baseline. Simulations that include freestream turbulence to initiate bypass transition will be explored in the final paper.

Figure 5 compares the isentropic Mach number obtained from the simulations at different spatial orders with the experimental data. The isentropic Mach number is defined as:

$$Ma_{is} = \sqrt{\frac{2}{\gamma-1}\left[\left(\frac{p_{t1}}{p}\right)^{\gamma-1/\gamma} - 1\right]}, \qquad (4)$$

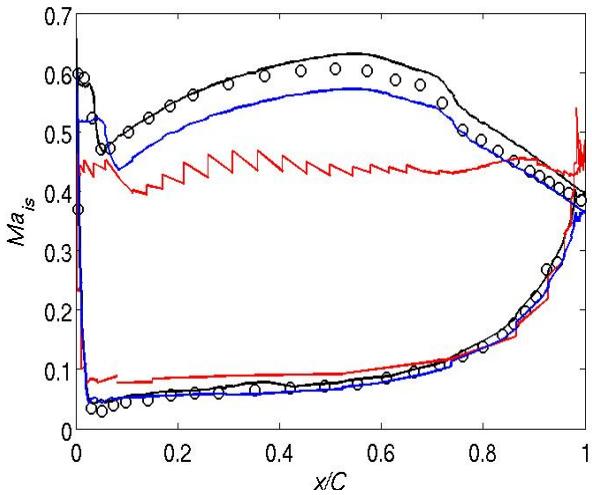

Figure 5. Comparison of isentropic Mach number between present simulations and experiments. Red line denotes 2nd order elements, blue 4th order, and black 8th order, and the circles represent experimental data.

For DG schemes, the numerical solutions are discontinuous at the element boundaries, which is most evident in the sawtooth profile of the 2nd-order simulation, indicating inadequate

resolution. With the increase of element spatial order, the resolution of the computed flowfield improves and the numerical solution converges to the experimental data on the pressure side and upstream portion of the airfoil. For the remainder of the paper, we will be concentrating on the 8^{th}-order solution.

In order to understand the discrepancy in computed pressure on the aft section of the airfoil suction side we examine the computed velocity field. Figure 6 presents the instantaneous local Mach number variation in the turbine cascade across the mid-span section of the domain. The flow remains attached and laminar on the pressure side, and the stagnation point is located at $x \approx 0.05C$. On the suction side the flow separates near the leading edge, and forms a small separation bubble (identified as a region of reversed flow). As the flow accelerates in the region $0 < x < 0.4C$, induced turbulence from the leading edge bubble decays. A similar leading-edge separation bubble was reported in [2] for a T106 blade with smaller pitch and inflow turbulence, and also in [16] for the T106A-EIZ configuration, both with and without freestream turbulence. As the flow decelerates on the aft portion of the airfoil suction side, another separation bubble forms at $x \approx 0.7C$. Flow downstream of this separation bubble becomes turbulent as a strong inflection point on the velocity profile occurs.

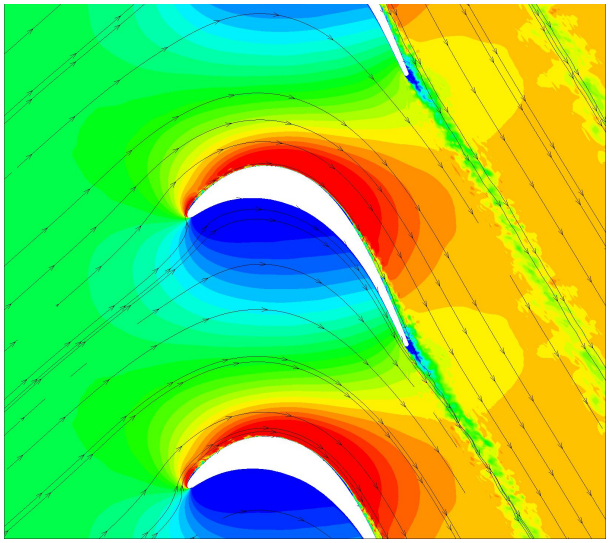

Figure 6. Instantaneous local Mach number profile across the mid-span section of the computational domain. Additional airfoils are periodically replicated for clarity.

Figure 7 presents the velocity field focused on the separated flow regions near the leading edge (Fig. 7a), and around the 70% axial chord location (Fig. 7b). It is evident from the discontinuous behavior of the velocity profiles near the aft separation location that the current 8^{th}-order simulation is still under-resolved. These thin, dynamic separation regions are sensitive to resolution and transition mechanism, both of which are lacking in these preliminary simulations. Ref. [11] reports the effect of freestream turbulence on the suction surface separation bubble for a similar T106A-EIZ turbine cascade (same airfoil geometry, but different pitch) and noted that the size of the separation bubble decreased with increasing freestream turbulence. The presence of the leading edge separation bubble was also reported in RANS-based simulations using transport-based transition models of the same T106D-EIZ configuration by Ref. [33]. Future work is aimed at a full mesh resolution study using both h and p refinement, similar to Fig. 1, in order to understand the efficiency improvements possible from higher-order methods, along with the bypass transition simulations mentioned earlier.

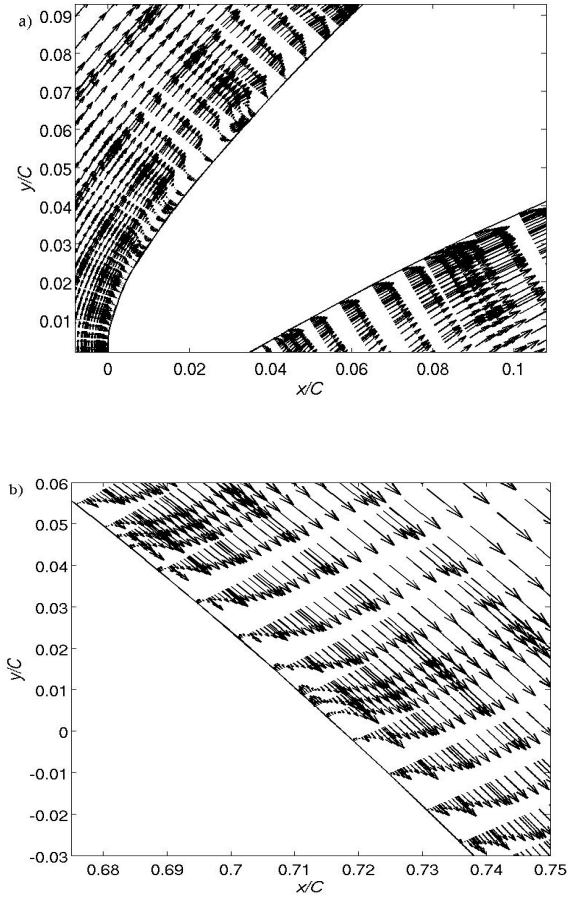

Figure 7. (a) Velocity vectors showing the leading edge separation bubble on the suction side of the airfoil. (b) Velocity vectors showing the aft region separation bubble on the suction side of the airfoil.

Fig. 8 shows the velocity magnitude (U) with respect to the tangential (ξ) and wall-normal (η) directions on the suction side of the turbine blade. The two separation bubbles on the suction side are also seen in Fig. 8, as denoted by the two dark blue regions at $\xi \approx 0.05C$ and $0.7C$. Aft of the second separation bubble, the boundary-layer thickness rapidly increases as the

flow becomes turbulent, whereas downstream of the first separation bubble the flow reattaches as it accelerates and the boundary-layer thickness decreases marginally. Although the location of the aft separation bubble matches the experiment, the boundary-layer thickness is underestimated in the numerical simulations. This under-estimation of the boundary-layer thickness is reflected in higher viscous losses, which in turn leads to a lower pressure ratio ($\frac{p_2}{p_1}$) across the cascade. The pressure ratio in the numerical simulation is calculated as 0.93 whereas the value from the experiments is 0.96. The smaller boundary-layer thickness in the vicinity of the separated flow region compared to the experimental data can also be seen in the velocity profiles at various locations on the suction surface shown in Fig. 9.

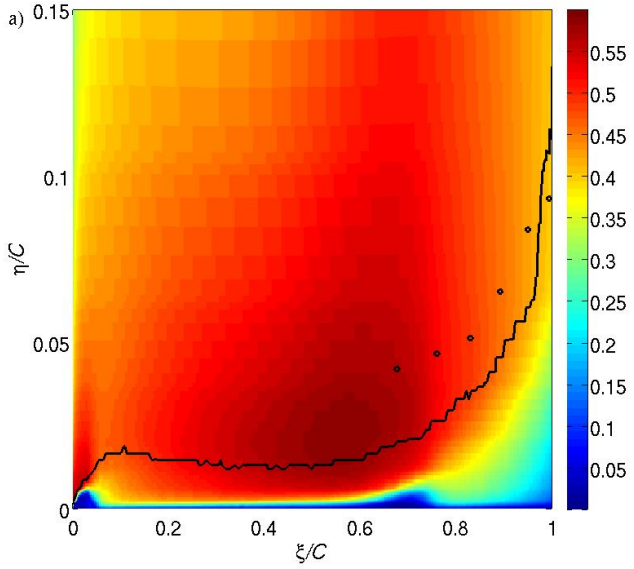

Figure 8. Velocity magnitude profile at midspan with respect to the tangential and wall-normal direction. Also shown is the boundary-layer thickness profile from the numerical simulations (solid black line) and experiments (circles).

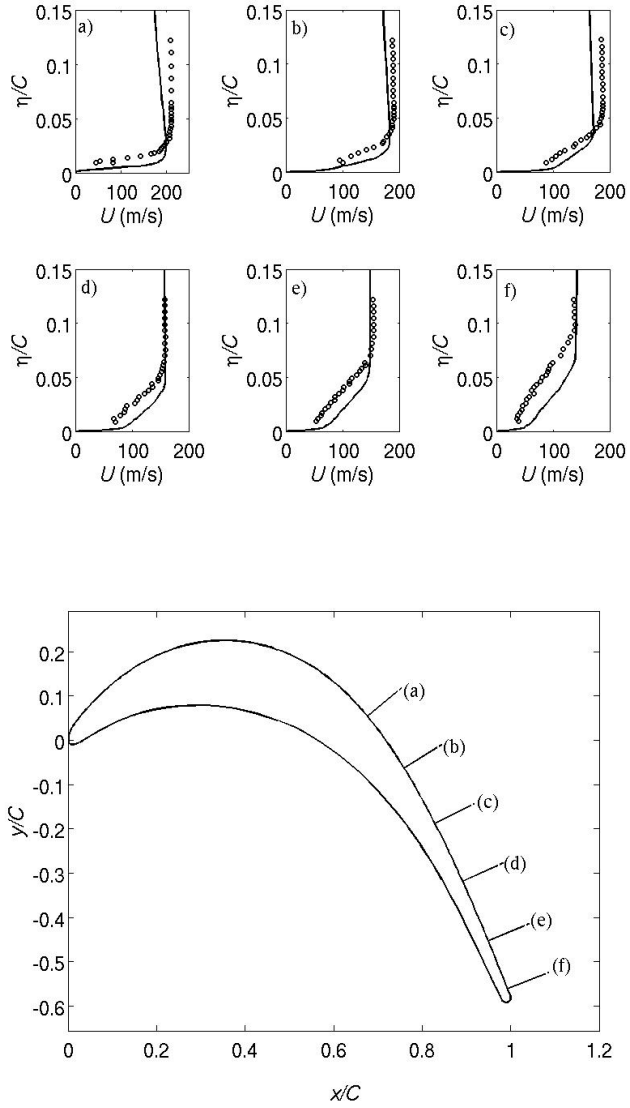

Figure 9. Comparison of velocity magnitude profile between experiment (circular marker) and numerical simulations (black solid line) at ξ = (a) 0.676C, (b) 0.7591C, (c) 0.8291C, (d) 0.8914C, (e) 0.9488C, (f) 0.993C. The locations along the airfoil surface corresponding to the velocity profile measurement locations are shown in the bottom figure for reference.

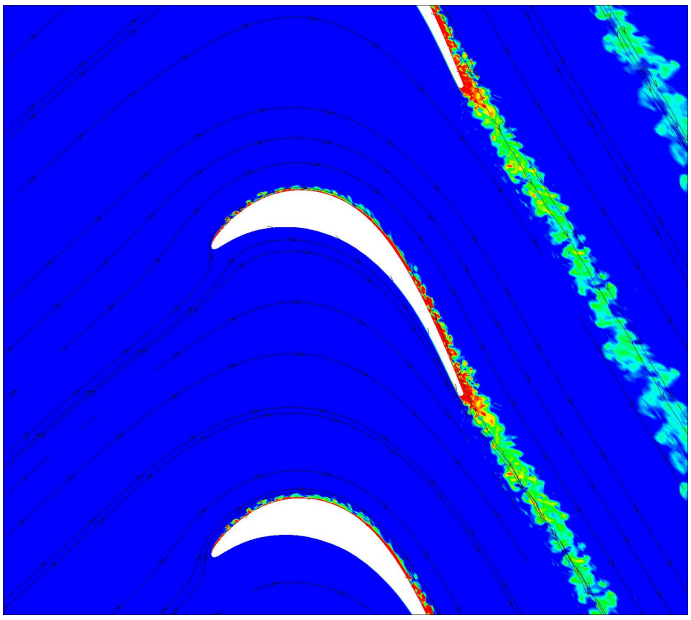

Figure 10. Instantaneous entropy profile across the midspan of computational domain. Additional airfoils are periodically replicated for clarity.

In order to better understand the flowfield around this low-pressure turbine stator, entropy profiles across the mid-span location are shown in Fig. 10. Due to the turbulent and laminar boundary layer on the suction and pressure side, both turbulent and laminar shear layers are observed very close to the trailing edge. Laminar vortex shedding from the pressure side undergoes laminar roll up, whereas on the suction side the roll up is less evident due to turbulence. Downstream from the trailing edge, the laminar and turbulent shear layer merge to form a fully turbulent wake (Fig. 10). Capturing the vortex-shedding phenomenon accurately in turbomachinery is important for predicting noise and rotor-stator interaction effects.

To examine the accuracy of the vortex shedding predictions, profiles of the total pressure loss in the wake are presented in Fig. 11.. The wake deficit is evaluated as the pressure loss coefficient:

$$\omega_u = \frac{p_{t1} - p}{p_{t1} - p_2}. \qquad (5)$$

In Fig. 11 the computed pressure loss coefficient is compared with the experiment results at 0.4C from the trailing edge. There is substantial scatter in the experimental data obtained using different measurement techniques. The wake deficit at such low Reynolds numbers is noted in the literature to be very difficult to accurately capture, particularly in RANS simulations with transition modeling. These RANS simulations generally underestimate the wake width and overestimate the pressure loss [24]. In the present DNS simulations, the estimated wake deficit compares reasonably well with the experiment. The wake loss profile is underestimated on the suction side, due to underestimation of the suction side boundary-layer thickness. The peak pressure loss is also underestimated by about 15%. The exit flow angle is estimated to be about 59° in the present simulations, while the experiments report a value of 63.2°.

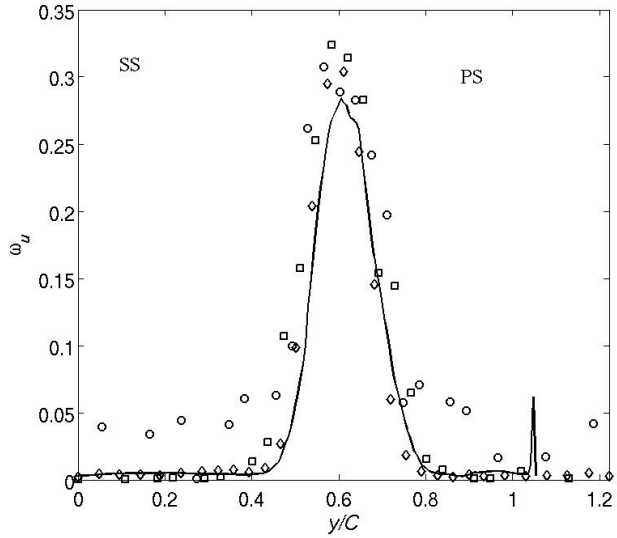

Figure 11. Comparison of wake loss profile between the experiment (circles from Kulite sensors, squares from pitot tube, diamonds from five-hole probe) and numerical results (black solid line). SS and PS denote the suction and pressure side, respectively.

CONCLUDING REMARKS

Preliminary results from a DNS of transitional and turbulent flow in a turbine stator cascade using a high-order entropy-stable DG spectral-element method with a space-time formulation are described. Isentropic Mach number profiles show that the pressure loading on the airfoil agrees well with the experiment, except in the aft region of the suction surface. Two separation bubbles are noted on the blade suction surface, one at the leading edge, and another at about 0.7C. The former separation bubble does not induce turbulence due to the flow acceleration in this region, while the latter is responsible for leading to turbulence in the aft region of the airfoil. Although the experiments were conducted with a nominal freestream turbulence intensity of 2.5%, the present simulations are performed assuming clean inflow conditions. This assumption can be expected to affect the results, by causing transition to occur through natural rather than bypass mechanisms, and may account for some of the discrepancies between the predicted results and the experiments. In particular, we note that the boundary-layer thickness is underestimated on the suction side aft region. This is also reflected in the wake loss profile comparison. The final paper will include additional numerical results, to study the effects of grid resolution and convergence, and freestream turbulence with detailed analysis of the flowfield.

We believe that the current computational methodology, as demonstrated by the validation study presented here, holds a lot of promise in predicting challenging and complicated turbomachinery flow phenomena. The combination of such high-order DG methods and their efficient implementation on modern high performance computing architectures can enable the routine use of high fidelity methods such as DNS and LES in the turbomachinery design process.

ACKNOWLEDGMENTS

Funding for Anirban Garai and Laslo Diosady was provided by the Fixed Wing and Aerosciences projects in the NASA Fundamental Aeronautics Program through the NASA Postdoctoral Program administrated by Oak Ridge Associated Universities (ORAU). The authors thank Stephan Stotz of the Institute of Jet Propulsion, UniBw Munich, for providing details regarding the experimental data and flow configuration.

REFERENCES

[1] Wu X, and Durbin PA, 2001. "Evidence of longitudinal vortices evolved from distorted wakes in a turbine passage," *J. Fluid Mech.*, **446**, pp. 199-228.

[2] Kalitzin G, Wu X, and Durbin PA, 2003. "DNS of fully turbulent flow in a LPT passage," *Int. J. Heat Fluid Flow*, **24**, pp. 636-644.

[3] Wissink JG, 2003. "DNS of separating, low Reynolds number flow in a turbine cascade with incoming wakes," *Int. J. Heat Fl.*, **24**, pp. 626-635.

[4] Wissink JG, and Rodi W, 2006. "Direct numerical simulation of flow and heat transfer in a turbine cascade with incoming wakes," *J. Fluid Mech.*, **569**, pp. 209-247.

[5] Zaki TA, Wissink JG, Rodi W, and Durbin PA, 2010. "Direct numerical simulation of transition in a compressor cascade: the influence of free-stream turbulence," *J. Fluid Mech.*, **665**, pp. 57-98.

[6] Rai MM, 2006. "A direct numerical simulation of transitional and turbulent flow on a turbine airfoil," 42nd AIAA/ASME/SAE/ASEE Joint Propulsion Conference & Exhibit, Nashville, TN.

[7] Rai MM, 2009. "A direct numerical simulation of transition and turbulence in a turbine stage," *47th AIAA Aerospace Science Meeting and Exhibit*, Orlando, Florida.

[8] Rai MM, 2010. "A direct numerical simulation of stator-rotor interaction in an axial compressor," 46th AIAA/ASME/SAE/ASEE Joint Propulsion Conference & Exhibit, Nashville, TN.

[9] Rai MM, 2011. "A direct numerical simulation of flow through a low pressure turbine stage," *41st AIAA Fluid Dynamics Conference and Exhibit*, Honolulu, Hawaii.

[10] Sandberg RD, Pichler R, Chen L, Johnstone R, and Michelassi V, 2014. "Compressible direct numerical simulation of low-pressure turbines: part I – methodology," *Proceedings of ASME Turbo Expo*, paper GT2014-2568, Dusseldorf, Germany.

[11] Michelassi V, Chen LW, Pichler R and Sandberg RD, 2014. "Compressible direct numerical simulation of low-pressure turbines: part II – effect of inflow disturbances," *Proceedings of ASME Turbo Expo*, paper GT2014-25689, Dusseldorf, Germany.

[12] Michelassi V, Wissink JG, Frohlich J, and Rodi W, 2003. "Large-eddy simulation of flow around low-pressure turbine blade with incoming wake". *AIAA J.*, **41**, pp. 2143-2156.

[13] Raverdy B, Mary I, Sagaut P, and Liamis N, 2003. "High-resolution large-eddy simulation of flow around low-pressure turbine blade". *AIAA J.*, **41**, pp. 390-397.

[14] Matsuura K, and Kato C, 2007. "Large eddy simulation of compressible transitional cascade flows in a low-pressure turbine cascades," *AIAA J.*, **45**, pp. 442-457.

[15] Sarkar S, and Voke, PR, 2006. "Large-eddy simulation of unsteady surface pressure over a low-pressure turbine blade due to interaction of passing wakes and inflexional boundary layer". *J. Turbomach.*, **128**, pp. 221-231.

[16] Medic G, and Sharma O, 2012. "Large-eddy simulation of flow in a low-pressure turbine cascade," *Proceedings of ASME Turbo Expo*, paper GT2012-68878, Copenhagen, Denmark.

[17] You D, Wang M, Moin P, and Mittal R, 2007. "Large-eddy simulation analysis of mechanisms for viscous losses in a turbomachinery tip-clearance flow," *J. Fluid Mech.*, **586**, pp. 177-204.

[18] Mishra A, and Bodony DJ, 2013. "Evaluation of actuator disk theory for predicting indirect combustion noise," *J. Sound Vibration*, **332**, pp. 21-38.

[19] Bassi F, Crivellini A, Rebay S, Savini M, 2005. "Discontinuous Galerkin solution of the Reynolds-averaged Navier–Stokes and k–x turbulence model equations," Computers & Fluids, **34**. pp. 507–540.

[20] Corsini A, Rispoli F, Santoriello A, 2005. "A variational multiscale higher-order finite-element formulation for turbomachinery flow computations," Comput. Methods Appl. Mech. Engr. 194, pp. 4797–4823.

[21] Cherednichenko S, Frey C, and Ashcroft G, 2012. "On the application of the Discontinuous Galerkin method to turbomachinery flows," European Congress on Computational Methods in Applied Sciences and Engineering (ECCOMAS 2012). J. Eberhardsteiner et.al. (eds.) Vienna, Austria.

[22] Ghidoni A, Colombo A, Rebay S, 2013. "Simulation of the transitional flow in a low pressure gas turbine cascade with a high-order Discontinuous Galerkin method," J. Fluids Eng. **135**, 071101.

[23] De Wiart CC, Hillewaert K, and Geuzaine P, 2012. "DNS of a low pressure turbine blade computed with a discontinuous Galerkin method," *Proceedings of ASME Turbo Expo*, paper GT2012-68900, Copenhagen Denmark.

[24] Hillewaert K, Verheylewegen G, and Arts T, 2014. "Assessment of a high-order discontinuous galerkin method for the direct numerical simulation of transition at low-reynolds number in the T106C high-lift low pressure turbine cascade," *Proceedings of ASME Turbo Expo*, paper GT2014-26739, Dusseldorf, Germany.

[25] Diosady LT, and Murman SM, 2013. "Design of a vibrational multiscale method for turbulent compressible flows," *AIAA*, paper 2013-2870.

[26] Diosady LT, and Murman SM, 2014. “DNS of flows over periodic hills using a discontinuous-Galerkin spectral-element method,” *44th AIAA Fluid Dynamic Conference*, Atlanta, Georgia, USA.
[27] Murman SM, Diosady LT, and Garai A, 2014. “Development of dynamic sub-grid modeling for variational multiscale methods”. Proceedings of the Summer Program 2014, Center for Turbulence Research, Stanford University, Stanford, CA.
[28] Stadtmuller P, and Fottner L, 2001. “A test case for the numerical investigation of wake passing effects on a highly loaded LP turbine cascade blade,” *Proceedings of ASME Turbo Expo*, Paper 2001-GT-0311, New Orleans, Louisiana, USA.
[29] Hughes TJR, Franca L, and Mallet M, 1986, “A new finite element formulation for computational fluid dynamics: I symmetric forms of the compressible Euler and Navier-Stokes equation and the second law of thermodynamics,” *Comput. Methods Appl. Math.*, **54**, pp. 223-234.
[30] Ismail F, and Roe PL, 2009. “Affordable, entropy-consistent Euler flux functions II: entropy production at shocks,” *Comput. Phys.*, **228**, pp. 5410-5436.
[31] Bassi F, and Rebay S, 2000. “GMRES discontinuous Galerkin solution of the compressible Navier-Stokes equations,” *Discontinuous Galerkin Methods: Theory, Computation and Applications*, edited by K. Cockburn and Shu, Springer, Berlin, pp. 197-208.
[32] Cardamone P, Stadmuller P, and Fottner L, 2002. “Numerical investigation of the wake-boundary layer interaction on a highly loaded lp turbine cascade blade,” *Proceedings of ASME Turbo Expo*, paper GT-2002-30367, Amsterdam, Netherlands.
[33] Blaim F, and Niehuis R, 2012. “Unsteady simulation of the LP turbine testcase T106D-EIZ using a transport equation based transition model,” Proceedings of Deutscher Luft- und Raumfahrtkongress.